Experimental and DFT study of GO-decorated CaO quantum dots for catalytic dye degradation and bactericidal potential

Mahreen Khan[1], Muhammad Ikram[1]*, Ali Haider[2],
Anwar Ul-Hamid[3], Hameed Ullah[4], Iram Shahzadi[5], Sherdil Khan[4],
Mohammed Benali Kanoun[6], Souraya Goumri-Said[7],
Francisco Medina[8] and Walid Nabgan[8]*

[1]Solar Cell Applications Research Laboratory, Department of Physics, Government College University Lahore, Lahore, Punjab, Pakistan, [2]Department of Clinical Sciences, Faculty of Veterinary and Animal Sciences, Muhammad Nawaz Shareef University of Agriculture (MNSUA) Multan, Multan, Pakistan, [3]Center for Engineering Research, Research Institute, King Fahd University of Petroleum and Minerals, Dhahran, Saudi Arabia, [4]Laboratory of Nanomaterials for Renewable Energy and Artificial Photosynthesis (NanoREAP), Institute of Physics, UFRGS, Porto Alegre, Rio Grande do Sul, Brazil, [5]Punjab University College of Pharmacy, University of the Punjab, Lahore, Pakistan, [6]Department of Mathematics and Sciences, College of Humanities and Sciences, Prince Sultan University, Riyadh, Saudi Arabia, [7]Physics Department, College of Science and General Studies, Alfaisal University, Riyadh, Saudi Arabia, [8]Departament d'Enginyeria Química, Universitat Rovira i Virgili, Tarragona, Spain

This research lays the groundwork for preparing graphene oxide (GO)-doped CaO nanocomposites for efficient antibacterial potential and dye degradation. The study aimed to reduce the recombination rate of the electron hole (e^-/h^+) of CaO and improve charge transfer. This issue can be minimized by doping high-surface area GO into CaO quantum dots (QDs). Herein, the one-pot co-precipitation technique has prepared various concentrations (1, 3, and 5 wt%) of GO-doped CaO. Characterization techniques were used to investigate optical, elemental analysis, microstructural, functional, and morphological properties. The addition of GO into QDs showed excellent catalytic activity (CA) to control sample CaO against methylene blue (MB) in basic and acidic media compared to the neutral media. The synergistic effect of morphological alternation attributed to an increase in the mechanism of CA upon doping. Various concentrations of GO to QDs promised remarkable bactericidal potency against *Escherichia coli*.

KEYWORDS

graphene oxide, CaO, antibacterial activity, catalysis, DFT

1 Introduction

Water is a fundamental requirement and crucial for the survival of life. The exponential growth of the global population and industrialization has caused the excessive use of water reservoirs (Vanthana Sree et al., 2020). The increase in population has led to several issues in our daily lives; water is contaminated by population growth in different ways, resulting in a threat to the ecosystem, and dyes play a vital role in water pollution (Chakraborty et al., 2021). Hazardous organic dyes are regularly generated from various industries such as paper, leather, food, textiles, and cosmetics (Alzahrani et al., 2021). Every year production rate of dyes is 7×10^5 to 1×10^6 tons (Chakraborty et al., 2021). A considerable amount of water is required for dying in textile industries, and 50% of water is discharged containing dye

contaminants. Reactive dyes and chemicals in wastewater are noxious, low biodegradable, and pose a major risk to the ecological system (Fatimah et al., 2011). The existence of these effluents could lead to destroying aquatic fauna and flora (Azad et al., 2015). Reactive dyes such as methylene blue (MB) possess the chemical formula $C_{16}H_{18}N_3SCl$ (319.85 g·mol^{-1}), and heterocyclic aromatic molecular structure has genotoxic nature. On account of different concentrations of MB, numerous disorders have been determined, for instance, chest pain, hemolysis, vomiting, hypotension, and fever (Jing et al., 2014; Nguyen et al., 2021). Through conventional approaches, dye effluents are not easily degraded because benzene rings are present (Walter et al., 2010; Walter et al., 2011). To eliminate pollutants from the discharge water, different methodologies that include adsorption, membrane filtration, and ion exchange, including coagulation, have been adopted (Subramanian et al., 2022). These technologies are cheaper but need continuous maintenance (Nigam et al., 2000). Compared to the approaches mentioned previously, catalytic remediation has gained significant attraction because of its cost favorable, easily manageable, and beneficial properties to oxidize dangerous organics (Dou et al., 2020; Hassan et al., 2020). The financial cost of mastitis is substantial on dairy zones. This disease is produced by infectious organisms like fungi, bacteria, and viruses. Microbiological and chemical changes in milk are ascribed as the irritation in mammary tissues and connected to this illness (Bari et al., 2022). Mastitis is caused by most prevailing pathogens *E. coli*, coliform, and *S. aureus* (Bari et al., 2022).

Nanotechnology is growing momentously in advanced research and rises with the evolution of NPs with promised microbicidal potential against multidrug-resistant microbes, implying a route to oppose microbial mutation arch (Roy et al., 2019). Particles with sizes ranging from 1 to 100 nm are considered nanoparticles (NPs) (Fard et al., 2015). Compared to bulk materials, NPs are highly sensitive, possess astonishing surface ratio to mass, and present unique characteristics like electrical, magnetic, and thermal properties. NPs are categorized into nanowires, nanotubes (multi-walled and single-walled), metals, and metal oxides (ZnO, CeO$_2$, TiO$_2$, CaO, etc.) (Gedda et al., 2015; Singh et al., 2020). Currently, CaO NPs captivated the focus of researchers due to their application in biocidal and prospective utilization in industries like high temperature, gas sensors, superconductors, and solar cells (Singhal et al., 2011). CaO NPs are particularly effective against bacteria and can render microbial endotoxins inactive (Sawai, 2003; Wang et al., 2017). CaO NPs can be exploited as drug delivery agents in photo-thermal therapy (PTT), photodynamic therapy (PDT), and synaptic delivery of chemotherapeutic drugs manifest to their particular phase and optical features (Butt et al., 2015; Singh et al., 2020). A thin sheet of hexagonally arranged carbon atoms bonded by sp^2 hybridization is known as graphene. It possesses allotropes such as GO and reduced graphene oxide (rGO) (Fan et al., 2021). Up to now, GO is a remarkable candidate to enhance semiconductors' photo-induced response because of its exceptional biocompatibility, high adsorption, immense surface area, low E$_g$, thermal conductivity, and low density (Munawar et al., 2022). Increasing photocatalytic potency from GO-doped metal oxides helps in the antimicrobial mechanism by producing more ROS (Karthik et al., 2017).

FIGURE 1
(A) Schematic representation of GO synthesis and **(B)** GO-doped CaO QDs.
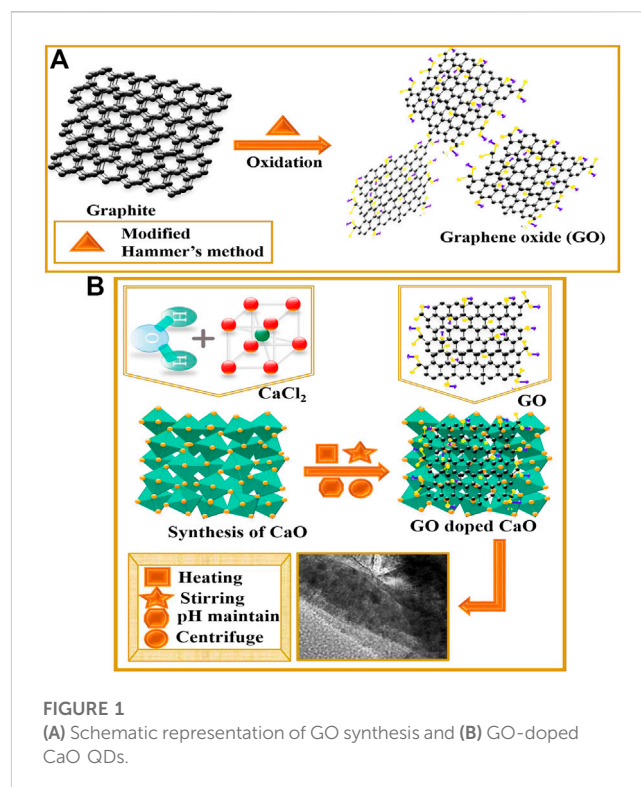
In this research, we have prepared GO-doped CaO QDs, adopting a facile co-precipitation route. The study followed synthesized specimens to assess the MB removal and bactericidal behavior. Furthermore, the dopant-dependent properties of CaO were analyzed, employing a variety of characterizations.

2 Experimental details

2.1 Materials

Calcium chloride dehydrates (CaCl$_2$·2H$_2$O, 99%), sodium hydroxide (NaOH, 98%), graphite powder (99%), and sodium nitrate (NaNO$_3$, 99.9%) were procured from Sigma-Aldrich. Sulfuric acid (H$_2$SO$_4$, 37%) and phosphoric acid (H$_3$PO$_4$) were obtained from Analar. Potassium permanganate (KMnO$_4$, 99%) and hydrochloric acid (HCl) were acquired from Merck. All reagents were utilized without additional purification.

2.2 Synthesis of graphene oxide (GO)

GO was synthesized from refined graphite *via* the modified Hummer method (Zaaba et al., 2017). Initially, graphite (5 g) and NaNO$_3$ (2.25 g) were incorporated in H$_2$SO$_4$ (108 mL) with H$_3$PO$_4$ (12 mL), and the resultant mixture was vigorously stirred for 10 min in a reaction flask immersed in an ice bath. Subsequently, the filtrate solution was poured into a muffle furnace for 120 min at 60 °C to remove moisture. Then, KMnO$_4$ (15 g) was introduced at > 5 °C gradually, and under strong stirring, the solution color turned from purple to yellow. In addition, 12 mL H$_2$O$_2$ was inserted and the

solution was centrifuged at 7,000 rpm for 7 min and repeatedly washed with DI water and HCl to obtain the residue. Accumulation was carried out for 12 h, and powder was achieved by grinding, as shown in Figure 1A.

2.3 Synthesis of GO-doped CaO QDs

To prepare CaO, an economically promising technique, co-precipitation, was proposed. First, 0.5 M of $CaCl_2.2H_2O$ was prepared under constant stirring. After 30 min, a colloidal solution was formed, and 1 M of NaOH was introduced drop by drop to maintain pH ~12 of the colloidal solution. The obtained precipitates from the colloidal solution were centrifuged (at 7,000 rpm for 7 min) twice with DI water to remove chloride and sodium impurities from the product and dried overnight at 70 °C. By adopting the aforementioned procedure, various concentrations (1, 3, and 5 wt%) of GO were doped into CaO solution and were synthesized and ground to achieve fine powder (Figure 1B).

2.4 Catalytic activity (CA)

Herein, CA has been employed to examine the degradation performance of MB in the presence of sodium borohydride ($NaBH_4$) and synthesized nanocatalysts (NCs). Initially, a solution of MB with a concentration of 10 g per 1000 mL was synthesized under robust stirring in a dark environment for 30 min. Then, 0.1 M stock solution of $NaBH_4$ was prepared, and ~400 μL of $NaBH_4$ solution was incorporated into the 3 mL aqueous solution of MB in a quartz cell. Afterward, 400 μL equipped host and (1, 3, and 5 wt%) GO-doped CaO QDs were added to the quartz cell. The integration of $NaBH_4$ and prepared NCs in MB solution improves the de-colorizations of the dye. The progress of degradation was monitored through a UV-vis spectrophotometer between 200 and 800 nm after a regular time interval. Specimens free of NCs had been called blank. The removal capability (%) was computed as follows:

$$Removal\ (\%) = \frac{Co - Ct}{Co} \times 100, \qquad (1)$$

where C_o refers to the initial absorbance and C_t represents the time-varying MB concentration.

2.5 Isolation and identification of MDR *E. coli*

2.5.1 Sample collection
From preferred milch cows sold at various markets and livestock amenities in Pakistan, bovine milk specimens were acquired through direct milking in sterile vitreous. After being collected at 4 °C, raw milk was instantly delivered to laboratories. On MacConkey agar, coliforms found in raw milk were counted, and all dishes were incubated at 37 °C for 48 h.

2.5.2 Recognition and characterization of bacterial isolates
According to Bergey's Manual of Determinative Bacteriology, the initial recognition of *E. coli* was centered on colony morphology by Gram staining and various biochemical tests (Haider et al., 2020a).

2.5.3 Antibiotic susceptibility
Mueller–Hinton agar (MHA) was used for the disk diffusion method to perform the antibiotic susceptibility test (Haider et al., 2020b). The test was conducted to find out whether *E. coli* was resistant to the successive antibiotics: azithromycin (Azm) 15 μg (macrolides), imipenem (Imi) 10 μg (carbapenem), ceftriaxone (Cro) 30 μg (cephalosporins), tetracycline (Te) 30 μg (tetracyclines), ciprofloxacin (Cip) 5 μg (quinolones), amoxicillin (A) 30 μg (penicillin), and gentamicin (Gm) 10 μg (aminoglycosides) (Adzitey et al., 2022). Standard colonies were cultured and balanced to 0.5 McFarland turbidity. After that, it was cultivated on MHA (Oxoid Limited, Basingstoke, United Kingdom), and antibiotic disks were positioned far enough away from the inoculation plate to prevent the overlap of the inhibition zone. Following the Clinical and Laboratory Standard Institute's interpretation of the data, Petri dishes were incubated at 37 °C overnight (NCCLS, 2007).
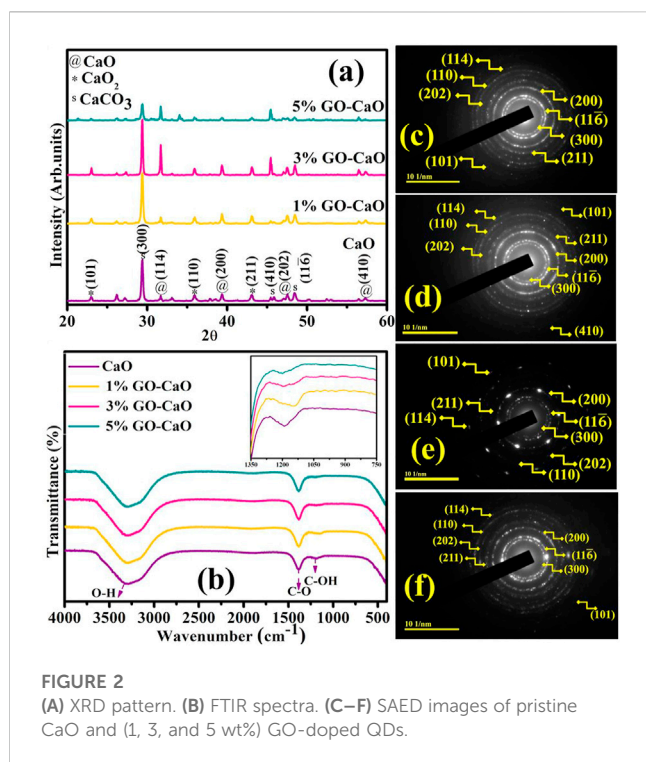
2.5.4 Antimicrobial activity
The bactericidal effect has modified a condition where an active ingredient alters the activeness of microorganisms. Antimicrobial competence of GO-doped CaO was assessed by employing the well diffusion methodology with Gram staining after swabbing 1.5 × 10^8 CFU·mL^{-1} Gram-negative (G^{-ve}) on MA distinctively. Furthermore, DIW (50 μL) and ciprofloxacin (0.005 mg/50 μL) were allocated as negative and positive roles, respectively. With the assistance of a micropipette and sanitized borer, various concentrations of CaO and GO (1, 3, and 5%)-doped CaO have been inoculated into wells of 6 mm diameter at low (0.5 mg/50 μL) and high (1.0 mg/50 μL) doses. Utilizing the Vernier calliper, inhibitory areas were measured in millimeters (mm) to assess the antibacterial efficiency after incubating loaded Petri dishes overnight.

2.5.5 Statistical analysis
Statistical analysis of the inhibitory zone diameters was determined utilizing SPSS 20 one-way analysis of variance (ANOVA). The inhibitory zone (mm) size was used to calculate the antibacterial efficacy (Haider et al., 2020b).

2.6 Characterizations of prepared specimens

High-resolution transmission electron microscopy HR-TEM, JEM2100F, JEOL, Japan, and FESEM (JSM-6460LV) combined with the EDX spectrometer has been utilized to assess the morphology, interlayer d-spacing, and elemental analysis, respectively, of prepared doped CaO. The A PerkinElmer 3100 FTIR spectrometer was used to attain the infrared spectra of the as-prepared samples. The crystallographic nature of CaO and GO-doped CaO was verified using a PAN analytical X'pert PRO powder diffractometer using monochromatic Cu-K$_\alpha$ radiation (λ ~ 0.0154 nm) ranging 2θ (20°–60°). A JASCO FP-8300 instrument was carried out on synthesized samples to perform PL

FIGURE 2
(A) XRD pattern. **(B)** FTIR spectra. **(C–F)** SAED images of pristine CaO and (1, 3, and 5 wt%) GO-doped QDs.

spectrophotometry. The electronic spectroscopy LABDeX with a range of 200–600 nm was employed to investigate the optical characteristics of the samples.

3 Results and discussion

The prepared GO with different concentrations (1, 3, and 5 wt%) was doped in synthesized CaO quantum dots using economic and low-temperature co-precipitation techniques, as shown in Figure 1.

Synthesized QDs were analyzed using XRD to obtain details regarding phase purity, crystallite size, and crystallographic planes in the 2θ (20°–60°) range. The XRD patterns of the synthesized product with different concentrations of GO are shown in Figure 2A. The characteristics peaks sited at 2θ values of 31.5, 39.5, 47.5, and 56.6° analogous to indexed diffraction (114), (200), (202), and (410), supporting the existence of CaO cubic structure authenticated by (ICDD Card No.00-017-0912, JCPDS File No. 37-1497) (Ikram et al., 2022a). Flexing of the Bragg peak revealed at 22.9° (101), 35.5° (110), and 43.0° (211) confirmed CaO_2 exhibiting tetragonal crystalline geometry validated with (JCPDS Card Nos. 01-085-0514, 00-003-0865). The minor peaks at 29.3°, 45.4°, and 48.5° were identified as (300), (410), and 11 $\overline{6}$ crystal planes, CaO appreciating as $CaCO_3$ ascertained to this band collection and synchronized with (JCPDS Card No. 083-1923, JCPDS Card No.00-047-1743). The absenteeism of the GO peak in the GO-doped CaO QDs certifies the CaO preferential orientation was unaltered by the addition of GO, resulted in the destruction of the GO normal layer-stacking, and might be the result of a small quantity of GO and reduced diffraction intensity (Liu et al., 2012; Liu et al., 2013). It was perceived that the Bragg peak intensity reduced as the dopant percentage increased (5 wt%), affirming the

little loss in crystallinity attributed to lattice disfigurement (Pradeev raj et al., 2018). Peak sharpness was substantial at lower percentages (1 and 3 wt%) of GO contents that preferred CaO QDs are adequately anchored with GO (Munawar et al., 2022).

Chemisorbed species, elemental constituents, and functional group assessment in the product molecules were manifested by non-destructive FTIR analysis. Corresponding spectra were ascertained in the frequency range 400–4000 cm^{-1}, as elaborated in Figure 2B. The broadband centering at 3300–3500 cm^{-1} can be associated with stretching the absorbed hydroxyl group (Raza et al., 2015). The sharp transmittance band at 1400 cm^{-1} exposes the C–O bond assigned to the carbonation of CaO QDs; this carbonation might be attributed to CO_2 in the atmosphere (Rojas et al., 2014; Ikram et al., 2022a). Peak flexing at ~ 1183 ascribed the (C–OH) starching (Oppong et al., 2017). The transmittance peak found at ~ 437 cm^{-1} related to the (C–H) stretching and at 540 cm^{-1} specified the Ca–O bond, certifying the formation of CaO QDs, as illustrated in Supplementary Figure S4 (Tangboriboon et al., 2012; Nano and Characterization, 2014). GO doping led to the shifting of transmittance band, as demonstrated in the inset of Figure 2. It has been documented that variations in shape, size, and local defects of NPs are responsible for the alteration noticed in the position and width of FTIR peaks (Saleh et al., 2016).

Following SAED analysis, attained concentric rings of CaO and GO-doped CaO elaborate the phase purity and crystalline nature depicted in Figures 2C–F. These rings were identified as reflection planes correlated with XRD measurements, proposing the cubic phase and poly-crystallinity of QDs.

Optical transition and details regarding the band structure and band shifting of QDs were extracted from electronic spectroscopy (Figure 3A). From the figure, CaO exhibited an absorbance band around 260–310 nm (Ramola and Joshi, 2019) with a considerable absorption edge at 286 nm credited to the transfer of electrons from Ca 4s into the 2p orbit of O, leading to the production of Ca^{2+} and O^{2-} ions and might be attributed to π–π* transition of C=C bonds (Skrabania et al., 2011; Jaiswal et al., 2021; Nguyen et al., 2021). The pristine GO presented a strong absorption in the range 250–280 nm with λ_{max} 265 nm manifested to the π–π* transition of C–C bonds, revealing the substantial conjugated structure of sp^2 carbons had been restored (Kumar et al., 2019). The addition of GO caused the shifting of the CaO absorbance band toward a longer wavelength (red-shift), manifested in the morphologic features containing a variety of active sub-levels; it could be the quantum confinement effect. Band gap energy (E_g) of NCs was evaluated by the Tauc plot, as shown in Eq. 2.

$$\alpha h\nu = D\left(h\nu - E_g\right)^n, \qquad (2)$$

where α, E_g, ν, and D represent the absorption coefficient, band gap, frequency of light, and constant sequentially, respectively, and $n = 2$ allow the indirect transition. The Tauc plot displayed the E_g of CaO and bare GO was 4.2 and 2.7 eV on the basis of extrapolating the linear part of curve to abscissa axis ($h\nu$) (Hidayah et al., 2017; Osuntokun et al., 2018), while the addition of GO (1, 3, and 5 wt%) to CaO showed a gradual decrease in the band gap energy 4.17, 4.11, and 4.07 eV,
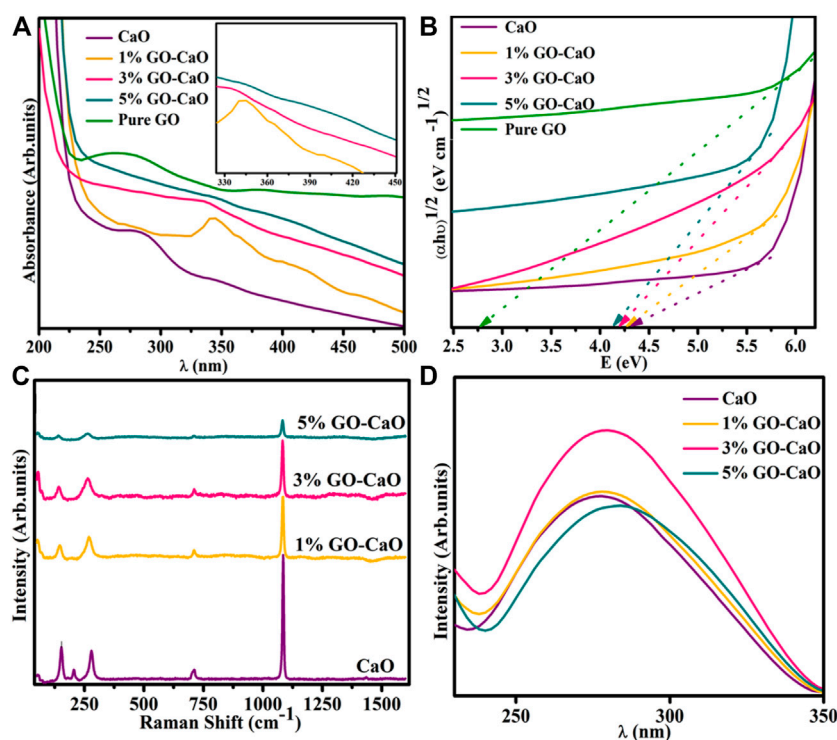
FIGURE 3
(A) Electronic spectra (inset graph); **(B)** E_g plot of CaO, bare GO, and (1, 3, and 5 wt%) GO-doped CaO; **(C)** emission spectra; and **(D)** Raman spectra of the host and (1, 3, and 5 wt%) GO-doped QDs.

respectively (Figure 3B). By eliminating the Burstein–Moss effect, GO actually helped narrow E_g and caused the red absorption shifting (Nguyen-Phan et al., 2011; Li et al., 2012). The incorporation of GO decreases E_g by affecting the width of the CB and VB region with the development of multiple energy levels throughout the band gap (Karyaoui et al., 2021).

The prepared samples were examined through PL spectra ranging from 200 to 800 nm with an excitation wavelength of 274 nm (Figure 3C). CaO QDs delivered UV emission at ~277 nm (Sinha et al., 2020), attributed to irradiative recombination of excitons. Near band edge emission (NBE) is responsible for the UV emission band. UV emission is assigned to the free recombination of photo-induced e^- inside CB and h^+ in VB (Panigrahy et al., 2009). The recombination rate of excitons and the PL emission intensity are both directly related. The graph illustrates that PL intensity for CaO and 1% GO-doped CaO was quite similar, but 3% GO-doped CaO exhibited highest emission intensity. This trend suggests an enhancement in the e^-/h^+ recombination ratio in singly ionized oxygen vacancy (Ramya et al., 2016). It is noteworthy that emission intensity decreased with a favorable GO amount (5% GO-doped CaO) that can be assigned to the transportation of e^- from high energy levels to newly induced states (Ikram et al., 2021a). A drop in emission peak intensity occurred upon incorporating a high dopant concentration, indicating that the dopant reduced the recombination rate by effective charge separation (Zhu et al., 2004; Sood et al., 2015). According to PL outcomes, the GO decorated to CaO restricts the recombination of charge carriers

through trapping of excited e^-s that are present in CB of CaO and resulting in the enhancement of light-harvesting capability (Katsukis et al., 2012). Moreover, PL peaks upon doping of GO shifted toward a higher wavelength relative to pure; it might be the consequence of interactions between CaO and the carbonyl functional group of GO (Tahir et al., 2022). This shifting leads to a reduction in E_g, consistent with absorption spectra.

Raman spectroscopy is the most versatile technique to investigate the inclusion of dopant, crystallographic structure, and lattice flaws in the pristine lattice structure. The observed Raman spectra of synthesized samples are represented in Figure 3D; the associated bands found around 157, 280, 713, and ~1092 cm^{-1} confirmed the function of CaO contents. The peak at ~ 1092 cm^{-1} has been designated to be the $Ca(OH)_2$ compound (Yang et al., 2009). The peak at 713 cm^{-1} is attributed to the antisymmetric stretching and plane-bending modes of carbonate ions (Smirnov et al., 2017). The peak flexing around 157 and 280 cm^{-1} can be assigned to the lattice vibration region (Nguyen et al., 2021). A blue shift occurred in Raman peaks upon doping, suggesting oxygen vacancy (V_o), distortion, and surface-associated flaws. This shifting is also manifested in phonon dispersion (Munawar et al., 2022).

EDS analysis of GO-doped QDs, illustrated in Supplementary Figure S1A, showed the observed elements (Ca, O, and Cl) appeared uniformly scattered across the sample proportion with varying elemental concentrations indicated *via* distinctive coloring (Supplementary Figure S1B–D). The obtained EDS spectra depicted two intense peaks of Ca and O, showing the existence of Ca and O. Additionally, the Cl peak appeared due to the precursor
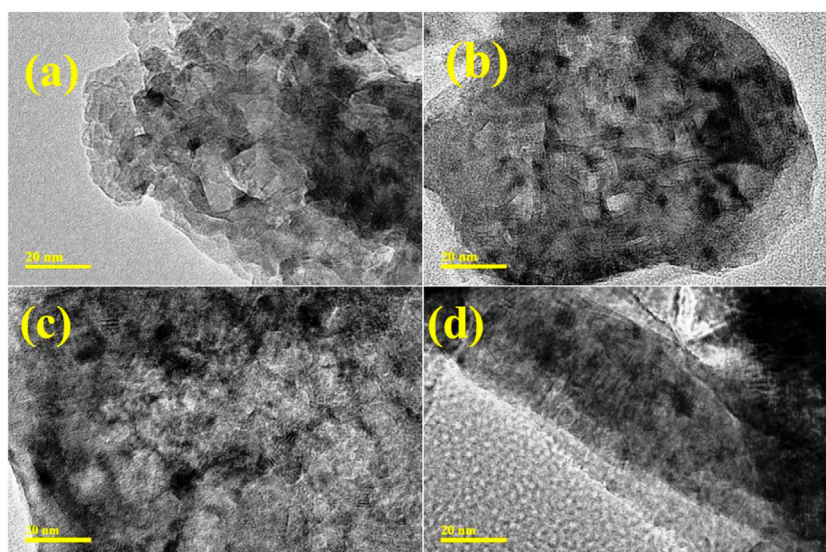
FIGURE 4
TEM images of **(A)** CaO and **(B–D)** GO-doped CaO at 1, 3, and 5 wt%, respectively.
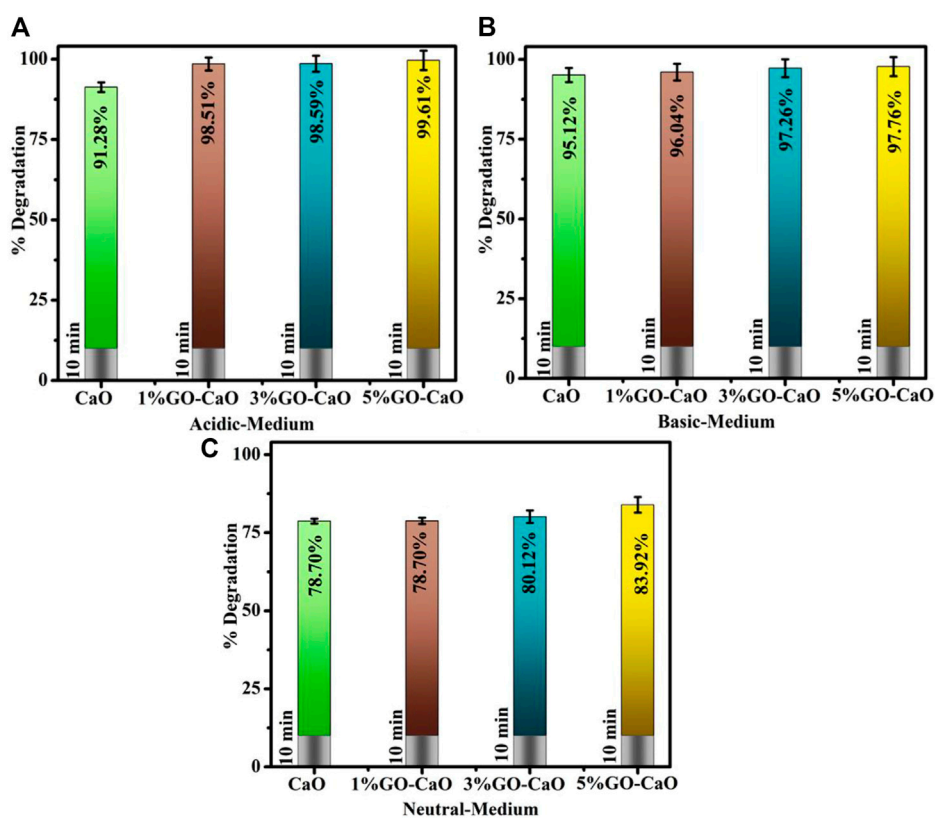

FIGURE 5
Catalytic activity of pristine and (1%, 3%, and 5%) GO-doped CaO in **(A)** acidic, **(B)** basic, and **(C)** neutral media.

utilized during the synthesis process of QDs. At 3.6 keV, a Ca peak emerged, and at 0.5 keV, the O peak was expressed.

TEM and HR-TEM analyses elucidated the topography of dopant-free and doped CaO. Figure 4A unveiled the agglomeration of the non-uniform formation of CaO QDs possessing an average calculated particle size of 9.786 nm. This agglomeration of QDs could be evident from the H-bonding of the solvent (DI water). GO (1%) was incorporated into CaO (Figure 4B), exhibiting the agglomerated overlapping of nanosheets with QDs accountable for nucleation growth. It was noted that with a higher concentration of GO (3%), QDs covered with a nanosheet exist in the coagulated form (Figure 4C). Figure 4D represented an aggregation upon the higher concentration of GO into QDs. Lattice fringes to be 0.22, 0.20, 0.18, and 0.19 nm for host and (1, 3, and 5 wt%) GO-doped QDs rendered through HR-TEM (Supplementary Figure S2A–D), which are compatible with XRD. TEM depicted that the GO sheet overlapped with QDs and matched well with HR-TEM as interlayer d-spacing decreased with the addition of GO.

The de-colorization of the dye was evaluated during CA when an electron was transferred from the oxidizing agent (MB) to the reducing agent (NaBH$_4$), stimulating an oxidation–reduction reaction (Supplementary Figure S3). However, the degradation of dye was time-consuming when MB was examined only in the presence of NaBH$_4$. To overwhelm this difficulty, pure and GO-doped CaO QDs were introduced in the redox reaction to operate as an electron relay and enable electron shifting from BH$_4^-$ to accepter MB. CA is significantly influenced by the surface area of the catalyst, crystallite size, and shape.

CA of pristine and doped-CaO was examined *via* UV-vis spectroscopy, as illustrated in Figures 5A–C. The pH of the solution was retained before adding NaBH$_4$ at 3 and 12 for acidic and basic MB by incorporating H$_2$SO$_4$ and NaOH, respectively. Host and (1, 3, and 5%) GO-doped CaO expressed the degradation in the acidic medium (pH = 4) 91.29, 98.51, 98.59, and 99.61%; in the basic medium (pH = 12) 95.12, 96.04, 97.26, and 97.76%; and in the neutral medium (pH = 7) 78.70, 78.70, 80.12, and 83.92% in 10 min, respectively. The results showed that the pH level of the solution reaction was an important factor in dye degradation. The significant degradation was observed upon doping of GO into QDs ascribed to the synergetic interaction between GO and CaO. The activity of GO-doped CaO was enhanced and manifested to the strong π–π conjugation with the chromophore group of the dye, high capacity for absorption of the dye, and lower e$^-$/h$^+$ recombination. These characteristics suggested that GO-doped CaO QDs played a vital role in the de-colorization of MB (Sreekanth et al., 2016). CA is affected by the nanocatalyst surface area, crystallite size, and shape. Generally, catalysts with a large surface area show higher catalytic efficiency as they offer more active sites. Moreover, the surface is usually large, but the impact of NCs is restricted because of microporosity, preventing reagents from diffusion to the active sites (Ikram et al., 2021b). The highest degradation was observed in an acidic medium, attributed to increased production of H$^+$ ions accessible for desorption on the NC surface (Ikram et al., 2021c). As previously reported, the dye degradation rate of certain azo dyes tends to increase as pH decreases (Alkaim et al., 2014). MB is a cationic dye and shows better efficiency in
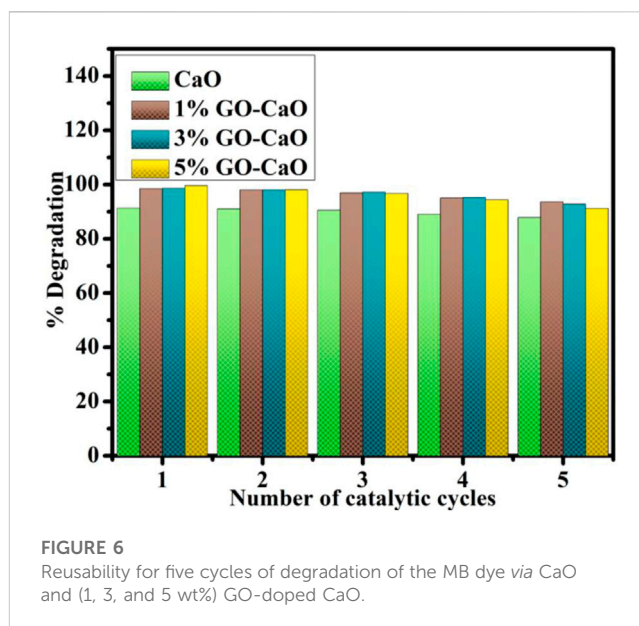

FIGURE 6
Reusability for five cycles of degradation of the MB dye *via* CaO and (1, 3, and 5 wt%) GO-doped CaO.

TABLE 1 Antibacterial activity of undoped and (1%, 3%, and 5%) GO-doped QDs.

Sample	Inhibition area (mm)	
	0.5 mg/50 µL	1.0 mg/50 µL
CaO	1.90	2.25
1% GO–CaO	2.65	3.95
3% GO–CaO	3.35	4.75
5% GO–CaO	5.85	7.10
Ciprofloxacin	5	5
DI water	0	0

the basic environment, attributed to strong electrostatic interactions between a negative catalyst charge and a dye (Meshkatalsadat et al., 2022). The results demonstrate that the removal efficacy of MB was relatively high in both basic and acidic media rather than in neutral medium ascribed to repulsion forces (Amanulla et al., 2022).

The repeatability of CA is significant since they enable industrial wastewater remediation for the maximum turns conceivable. The reusability of CaO and (1%, 3%, and 5%) GO-doped CaO QDs was tested through the recycling experiment (Figure 6). The NCs were separated from the reaction mixture, washed, and dried before each new cycle, while the other reaction conditions remain unchanged. After five turns, the reused catalysts presented a slight drop in the de-colorization rate of MB in terms of percentage. Catalysts are stable and can be reused for up to five turns. This demonstrates that the catalytic activity of reused catalysts provides reproducible dye degradation results. The production of by-products and their aggregation on the active sites of the catalysts may explain the reduction in de-colorization percentages between cycles.
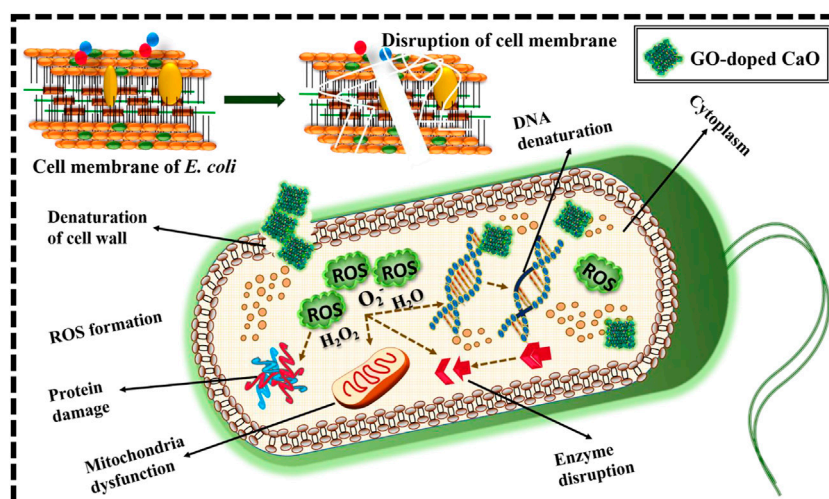
FIGURE 7
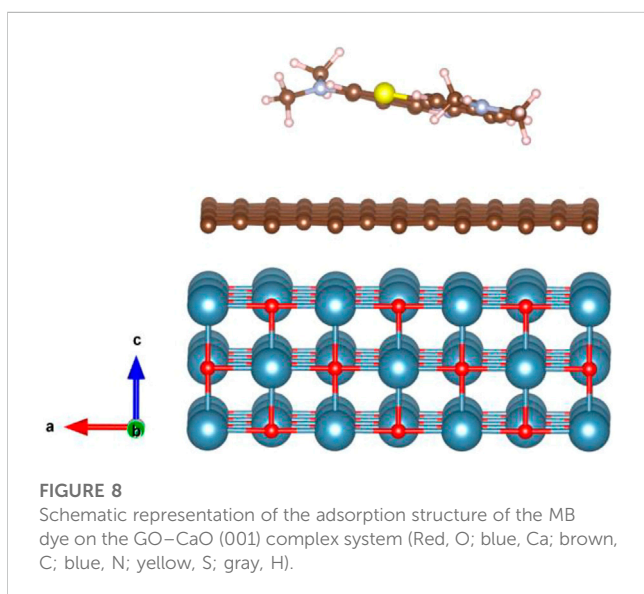Schematic representation of mechanism for antimicrobial activity of the prepared GO-doped CaO.

FIGURE 8
Schematic representation of the adsorption structure of the MB dye on the GO–CaO (001) complex system (Red, O; blue, Ca; brown, C; blue, N; yellow, S; gray, H).

In vitro microbicidal efficiency of prepared products was monitored from inhibition ranges (mm), adopting a well diffusion assay regarding *E. coli*. The inhibition zone was reported from (1.90–5.85) to (2.25–7.10) in *E. coli* at minimal and maximal doses, respectively. Table 1 disclosed promised antibacterial competence; furthermore, GO-doped QDs demonstrated considerable bacterial vulnerability relative to CaO. The credible justification for supreme bactericidal presentation with more percentage doping of GO is that GO produced oxidative stress on the biofilm and owned additional reactive groups, which might interact with the cell surface causing cell apoptosis (Sharma et al., 2020).

It could be inferred that the synergetic outcomes of CaO QDs depended upon the interaction between the host specimen and

bacterial cell wall. The enhancement in percentage effectiveness against G^{-ve} is inversely related to the NP size (Fan et al., 2021) as size plays a key role in the generation of ROS. CaO QDs possessed a large surface area to volume ratio that not only helped increase reactive oxygen species (ROS) formation but also gave adequate adhesion with microbiological constituents (Gedda et al., 2015). Productions of more ROS by small-sized QDs insert microorganism membrane devastation, and ultimately, cytoplasmic organelles encourage bacterial death (Fang et al., 2015; Qumar et al., 2020). Anionic microorganism membrane elements interact with sufficient Ca^{+2} responsible for superior bactericidal morality (Fang et al., 2015), as in Figure 7.

To gain a thorough understanding of the absorption behavior of the MB on GO—CaO composite, the structural relaxation calculations were performed with density functional theory (DFT) calculations using the QuantumATK package (Smidstrup et al., 2020) within the Perdew–Burke–Ernzerhof (PBE) (Perdew et al., 1996) formulation for the exchange–correlation energy functional. The DFT-D2 method of Grimme (2006) was applied to describe the long-range van der Waals forces between the CaO surface and graphene, and the MB and GO–CaO surface composite. Pseudo Dojo's (van Setten et al., 2018) norm-conserving pseudopotentials along with the corresponding linear combination of atomic orbital (LCAO) basis set of "medium" accuracy were used with a mesh cutoff energy of 125 Ha. Geometry optimization is performed using the LBFGS (limited-memory Broyden–Fletcher–Goldfarb–Shanno) optimizer with a force tolerance of 0.01 eV/Å. The Monkhorst–Pack method was used to sample the k-points of $4 \times 4 \times 1$ within a first Brillouin zone. The calculated lattice parameter of bulk cubic CaO is $a = 4.839$ Å, which is consistent with the experimental values ($a = 4.8105$ Å) (Mammone et al., 1981). The CaO (001) surface was modeled using a repeated slab model structure composed of a 3×3 surface unit cell. We used a significant vacuum height of 25 Å to exclude the interaction between adjacent slabs. The most stable surface, CaO (001), was considered the model for calculating MB adsorption

(Orazi et al., 2020; Ikram et al., 2022b). as shown in Figure 8. The adsorption energy of the MB on GO–CaO composite is calculated from the expression (Hassan et al., 2021; Ikram et al., 2022b), where $E_{MB+composite}$, $E_{composite}$, and E_{MBN} are the total energies of the MB adsorbed on the GO–CaO composite, GO–CaO complexes, and the isolated gas molecule, respectively. The calculated E_{ads} value is found to be −4.66 eV, confirming an exothermic adsorption energy and strong interaction between MB and the GO–CaO composite. For comparison, the E_{ads} of GO on CaO (001) was computed and equal to −2.94 eV.

4 Conclusion

Herein, pristine and (1, 3, and 5 wt%) GO-doped QDs were prepared by a simple co-precipitation technique to obtain an enhanced CA and antibacterial potential. According to XRD results, CaO, CaO_2, and $CaCO_3$ possessed FCC structures and were found to be crystalline in nature. FTIR unveiled characteristic peaks at 540 cm^{-1} corresponding to the CaO; EDS spectra confirmed the presence of dopants and CaO. A red shift was noticed with GO, resulting in a decrease of Eg from 4.2 to 4.07 eV. TEM analysis disclosed the non-uniform QDs morphology of CaO with an average particle size of 9.786 nm, and agglomeration increased with an increasing amount of the dopant. Interlayer d-spacing was computed as 0.22, 0.20, 0.18, and 0.19 nm from HR-TEM analysis. The PL study verified that a high dopant ratio suppressed the e$^-$/h$^+$ recombination that transpires to boost the catalytic activity. In view of the experimental findings, GO addition in CaO with 3 and 5 wt% presented the highest catalytic activity in an acidic medium, 98.59% and 99.61%. Overall, a higher concentration of GO showed significant microbicidal activity with zone diameters of 7.10 mm and 2.25 mm at a maximum dosage against the G^{-ve} pathogen.

Data availability statement

The datasets presented in this study can be found in online repositories. The names of the repository/repositories and accession number(s) can be found. Data are available by request.

Author contributions

MK: conceptualization, investigation, writing-original draft preparation, and visualization. MI: methodology, formal analysis, writing-review and editing, supervision, and funding acquisition. AH: conceptualization and resources. AU-H: investigation and data curation. HU: methodology and investigation. IS: formal analysis and resources. SK: conceptualization and data curation. MK: methodology and formal analysis. SG-S: investigation and formal analysis. FM: data analysis, interpretation, conceptualization, review and editing, investigation, formal analysis, and fund acquisition; WN: conceptualization, writing-review and editing, and investigation. All authors contributed to the article and approved the submitted version.

Conflict of interest

The authors declare that the research was conducted in the absence of any commercial or financial relationships that could be construed as a potential conflict of interest.

Publisher's note

All claims expressed in this article are solely those of the authors and do not necessarily represent those of their affiliated organizations, or those of the publisher, the editors, and the reviewers. Any product that may be evaluated in this article, or claim that may be made by its manufacturer, is not guaranteed or endorsed by the publisher.

Supplementary material

The Supplementary Material for this article can be found online at: https://www.frontiersin.org/articles/10.3389/fenvs.2023.1158399/full#supplementary-material

References

Adzitey, F., Yussif, S., Ayamga, R., Zuberu, S., Addy, F., Adu-Bonsu, G., et al. (2022). Antimicrobial susceptibility and molecular characterization of *Escherichia coli* recovered from milk and related samples. *Microorganisms* 10, 1335. doi:10.3390/microorganisms10071335

Alkaim, A. F., Aljeboree, A. M., Alrazaq, N. A., Baqir, S. J., Hussein, F. H., and Lilo, A. J. (2014). Effect of pH on adsorption and photocatalytic degradation efficiency of different catalysts on removal of methylene blue. *Asian J. Chem.* 26, 8445–8448. doi:10.14233/ajchem.2014.17908

Alzahrani, F. M., Alsaiari, N. S., Katubi, K. M., Amari, A., Ben Rebah, F., and Tahoon, M. A. (2021). Synthesis of polymer-based magnetic nanocomposite for multi-pollutants removal from water. *Polym. (Basel)* 13. doi:10.3390/polym13111742

Amanulla, M., Magdalane, C. M., Ramalingam, G., Sundaram, R., Tamam, N., Somaily, H. H., et al. (2022). Fabrication and characterization of Th(MoO4)2/ TiO2 nanocomposite for potential use in photocatalytic degradation of toxic pollutants. *Appl. Phys. A Mat. Sci. Process.* 128, 397. doi:10.1007/s00339-022-05504-1

Azad, A. K., Rasul, M. G., Mofijur, M., Bhuiya, M. M. K., Mondal, S. K., and Sattar, M. K. (2015). Energy and waste management for petroleum refining effluents: A case study in Bangladesh. *Int. J. Automot. Mech. Eng.* 11, 2170–2187. doi:10.15282/ijame.11.2015. 1.0182

Bari, A., Ikram, M., Haider, A., Ul-Hamid, A., Haider, J., Shahzadi, I., et al. (2022). Evaluation of bactericidal potential and catalytic dye degradation of multiple morphology based chitosan/polyvinylpyrrolidone-doped bismuth oxide nanostructures. *Nanoscale Adv.* 4, 2713–2728. doi:10.1039/d2na00105e

Butt, A. R., Ejaz, S., Baron, J. C., Ikram, M., and Ali, S. (2015). CaO nanoparticles as a potential drug delivery agent for biomedical applications, Dig. *J. Nanomater. Biostructures.* 10, 799–809. Available at: https://www.researchgate.net/profile/Riaz-Khan-3/post/How-we-can-calculate-drug-loading-on-NPs-through-Thermogravimetric-analysis-TGA/attachment/59d6337679197b8077991234/AS%3A374959902871553%401466408815669/download/799_Butt.pdf (accessed December 13, 2022).

Chakraborty, S., Mukherjee, A., Das, S., Maddela, N. R., Iram, S., and Das, P. (2021). Study on isotherm, kinetics, and thermodynamics of adsorption of crystal violet dye by calcium oxide modified fly ash. *Environ. Eng. Res.* 26, 1–9. doi:10.4491/eer.2019.372

Dou, R., Cheng, H., Ma, J., and Komarneni, S. (2020). Manganese doped magnetic cobalt ferrite nanoparticles for dye degradation via a novel heterogeneous chemical catalysis. *Mat. Chem. Phys.* 240, 122181. doi:10.1016/j.matchemphys.2019.122181

Fan, X., Yahia, L., and Sacher, E. (2021). Antimicrobial properties of the Ag, Cu nanoparticle system. *Biol. (Basel)* 10, 137–37. doi:10.3390/biology10020137

Fang, W., Chaofa, X., Zheng, J., Chen, G., and Jiang, K. (2015). Fabrication of Cu-Ag bimetal nanotube-based copper silicates for enhancement of antibacterial activities. *RSC Adv.* 5, 39612–39619. doi:10.1039/c5ra06065f

Fard, J. K., Jafari, S., and Eghbal, M. A. (2015). A review of molecular mechanisms involved in toxicity of nanoparticles. *Adv. Pharm. Bull.* 5, 447–454. doi:10.15171/apb. 2015.061

Fatimah, I., Wang, S., and Wulandari, D. (2011). ZnO/montmorillonite for photocatalytic and photochemical degradation of methylene blue. *Appl. Clay Sci.* 53, 553–560. doi:10.1016/j.clay.2011.05.001

Gedda, G., Pandey, S., Lin, Y. C., and Wu, H. F. (2015). Antibacterial effect of calcium oxide nano-plates fabricated from shrimp shells. *Green Chem.* 17, 3276–3280. doi:10. 1039/c5gc00615e

Grimme, S. (2006). Semiempirical GGA-type density functional constructed with a long-range dispersion correction. *J. Comput. Chem.* 27, 1787–1799. doi:10.1002/jcc. 20495

Haider, A., Ijaz, M., Ali, S., Haider, J., Imran, M., Majeed, H., et al. (2020). Green synthesized phytochemically (zingiber officinale and allium sativum) reduced nickel oxide nanoparticles confirmed bactericidal and catalytic potential. *Nanoscale Res. Lett.* 15, 50. doi:10.1186/s11671-020-3283-5

Haider, A., Ijaz, M., Imran, M., Naz, M., Majeed, H., Khan, J. A., et al. (2020). Enhanced bactericidal action and dye degradation of spicy roots' extract-incorporated fine-tuned metal oxide nanoparticles. *Appl. Nanosci.* 10, 1095–1104. doi:10.1007/ s13204-019-01188-x

Hassan, J., Ikram, M., Ul-Hamid, A., Imran, M., Aqeel, M., and Ali, S. (2020). Application of chemically exfoliated boron nitride nanosheets doped with Co to remove organic pollutants rapidly from textile water. *Nanoscale Res. Lett.* 15, 75. doi:10.1186/ s11671-020-03315-y

Hassan, J., Naz, S., Haider, A., Raza, A., Ul-Hamid, A., Qumar, U., et al. (2021). h-BN nanosheets doped with transition metals for environmental remediation; a DFT approach and molecular docking analysis. *Mat. Sci. Eng. B Solid-State Mat. Adv. Technol.* 272, 115365. doi:10.1016/j.mseb.2021.115365

Hidayah, N. M. S., Liu, W. W., Lai, C. W., Noriman, N. Z., Khe, C. S., Hashim, U., et al. (2017). "Comparison on graphite, graphene oxide and reduced graphene oxide: Synthesis and characterization," in *AIP conf. Proc.* (American Institute of Physics Inc.), 150005. doi:10.1063/1.5005764

Ikram, M., Haider, A., Bibi, S. T., Ul-Hamid, A., Haider, J., Shahzadi, I., et al. (2022). Synthesis of Al/starch co-doped in CaO nanoparticles for enhanced catalytic and antimicrobial activities: Experimental and DFT approaches. *RSC Adv.* 12, 32142–32155. doi:10.1039/d2ra06340a

Ikram, M., Hayat, S., Imran, M., Haider, A., Naz, S., Ul-Hamid, A., et al. (2021). Novel Ag/cellulose-doped CeO2 quantum dots for efficient dye degradation and bactericidal activity with molecular docking study. *Carbohydr. Polym.* 269, 118346. doi:10.1016/j. carbpol.2021.118346

Ikram, M., Inayat, T., Haider, A., Ul-Hamid, A., Haider, J., Nabgan, W., et al. (2021). Graphene oxide-doped MgO nanostructures for highly efficient dye degradation and bactericidal action. *Nanoscale Res. Lett.* 16, 56. doi:10.1186/s11671-021-03516-z

Ikram, M., Mahmood, A., Haider, A., Naz, S., Ul-Hamid, A., Nabgan, W., et al. (2021). Dye degradation, antibacterial and *in-silico* analysis of Mg/cellulose-doped ZnO nanoparticles. *Int. J. Biol. Macromol.* 185, 153–164. doi:10.1016/j.ijbiomac.2021.06.101

Ikram, M., Muhammad Khan, A., Haider, A., Haider, J., Naz, S., Ul-Hamid, A., et al. (2022). Facile synthesis of La- and chitosan-doped CaO nanoparticles and their evaluation for catalytic and antimicrobial potential with molecular docking Studies. *ACS Omega* 7, 28459–28470. doi:10.1021/acsomega.2c02790

Jaiswal, K. K., Dutta, S., Pohrmen, C. B., Verma, R., Kumar, A., and Ramaswamy, A. P. (2021). Bio-waste chicken eggshell-derived calcium oxide for photocatalytic application in methylene blue dye degradation under natural sunlight irradiation. *Inorg. Nano-Metal Chem.* 51, 995–1004. doi:10.1080/24701556.2020.1813769

Jing, H. P., Wang, C. C., Zhang, Y. W., Wang, P., and Li, R. (2014). Photocatalytic degradation of methylene blue in ZIF-8. *RSC Adv.* 4, 54454–54462. doi:10.1039/ c4ra08820d

Karthik, R., Vinoth Kumar, J., Chen, S. M., Karuppiah, C., Cheng, Y. H., and Muthuraj, V. (2017). A study of electrocatalytic and photocatalytic activity of cerium molybdate nanocubes decorated graphene oxide for the sensing and degradation of antibiotic drug chloramphenicol. *ACS Appl. Mat. Interfaces.* 9, 6547–6559. doi:10.1021/acsami.6b14242

Karyaoui, M., Ben Jemia, D., Daoudi, M., Bardaoui, A., Boukhachem, A., Amlouk, M., et al. (2021). Physical properties of graphene oxide GO-doped ZnO thin films for optoelectronic application. *Appl. Phys. A Mat. Sci. Process.* 127, 134. doi:10.1007/ s00339-020-04269-9

Katsukis, G., Malig, J., Schulz-Drost, C., Leubner, S., Jux, N., and Guldi, D. M. (2012). Toward combining graphene and QDs: Assembling CdTe QDs to exfoliated graphite and nanographene in water. *ACS Nano* 6, 1915–1924. doi:10.1021/nn204700z

Kumar, A., Sadanandhan, A. M., and Jain, S. L. (2019). Silver doped reduced graphene oxide as a promising plasmonic photocatalyst for oxidative coupling of benzylamines under visible light irradiation. *New J. Chem.* 43, 9116–9122. doi:10.1039/c9nj00852g

Li, B., Liu, T., Wang, Y., and Wang, Z. (2012). ZnO/graphene-oxide nanocomposite with remarkably enhanced visible-light-driven photocatalytic performance. *J. Colloid Interface Sci.* 377, 114–121. doi:10.1016/j.jcis.2012.03.060

Liu, L., Bai, H., Liu, J., and Sun, D. D. (2013). Multifunctional graphene oxide-TiO2-Ag nanocomposites for high performance water disinfection and decontamination under solar irradiation. *J. Hazard. Mat.* 261, 214–223. doi:10.1016/j.jhazmat.2013. 07.034

Liu, X., Pan, L., Zhao, Q., Lv, T., Zhu, G., Chen, T., et al. (2012). UV-assisted photocatalytic synthesis of ZnO-reduced graphene oxide composites with enhanced photocatalytic activity in reduction of Cr(VI). *Chem. Eng. J.* 183, 238–243. doi:10.1016/j. cej.2011.12.068

Mammone, J. F., Mao, H. K., and Bell, P. M. (1981). Equations of state of CaO under static pressure conditions. *Geophys. Res. Lett.* 8, 140–142. doi:10.1029/ GL008i002p00140

Meshkatalsadat, M. H., Zahedifar, M., and Pouramiri, B. (2022). Facile green synthesis of CaO NPs using the Crataegus pontica C.Koch extract for photo-degradation of MB dye. *Environ. Sci. Pollut. Res.* 29, 54688–54697. doi:10.1007/s11356-022-19671-4

M. G., Walter, E. L., Warren, J. R., McKone, S. W., Boettcher, Q., Mi, E. A., Santori, et al. (2011). Erratum: Solar water splitting cells. *Chem. Rev.* 111, 5815. doi:10.1021/ cr200102n

Munawar, T., Nadeem, M. S., Mukhtar, F., ur Rehman, M. N., Riaz, M., Batool, S., et al. (2022). Transition metal-doped SnO2 and graphene oxide (GO) supported nanocomposites as efficient photocatalysts and antibacterial agents. *Environ. Sci. Pollut. Res.* 29, 90995–91016. doi:10.1007/s11356-022-22144-3

Nano, C. A. O., and Characterization, P. T. (2014). SOL-GEL methodof synthesis ofmgo and cao nano particlesand their characterization, wjpr.S3.Ap-south-1. *Amaz. Com.* 3, 362–370. Available at: https://wjpr.s3.ap-south-1.amazonaws.com/article_issue/1410847401.pdf (accessed December 25, 2022).

NCCLS (2007). Performance standards for antimicrobial susceptibility testing. *Clin. Lab. Standars Inst.* 27, 1–182. doi:10.3/JQUERY-UI.JS

Nguyen, D. K., Van On, V., Hoat, D. M., Rivas-Silva, J. F., and Cocoletzi, G. H. (2021). Structural, electronic, magnetic and optical properties of CaO induced by oxygen incorporation effects: A first-principles study. *Phys. Lett. Sect. A Gen. At. Solid State Phys.* 397, 127241. doi:10.1016/j.physleta.2021.127241

Nguyen-Phan, T. D., Pham, V. H., Shin, E. W., Pham, H. D., Kim, S., Chung, J. S., et al. (2011). The role of graphene oxide content on the adsorption-enhanced photocatalysis of titanium dioxide/graphene oxide composites. *Chem. Eng. J.* 170, 226–232. doi:10. 1016/j.cej.2011.03.060

Nigam, P., Armour, G., Banat, I. M., Singh, D., and Marchant, R. (2000). Physical removal of textile dyes from effluents and solid-state fermentation of dye-adsorbed agricultural residues. *Bioresour. Technol.* 72, 219–226. doi:10.1016/S0960-8524(99) 00123-6

Oppong, S. O. B., Anku, W. W., Shukla, S. K., and Govender, P. P. (2017). Synthesis and characterisation of neodymium doped-zinc oxide–graphene oxide nanocomposite as a highly efficient photocatalyst for enhanced degradation of indigo carmine in water under simulated solar light. *Res. Chem. Intermed.* 43, 481–501. doi:10.1007/s11164-016-2636-2

Orazi, V., Juan, A., González, E. A., Marchetti, J. M., and Jasen, P. V. (2020). DFT study of ethanol adsorption on CaO(0 0 1) surface. *Appl. Surf. Sci.* 500, 144254. doi:10.1016/j.apsusc.2019.144254

Osuntokun, J., Onwudiwe, D. C., and Ebenso, E. E. (2018). Aqueous extract of broccoli mediated synthesis of CaO nanoparticles and its application in the photocatalytic degradation of bromocrescol green. *IET Nanobiotechnology* 12, 888–894. doi:10.1049/iet-nbt.2017.0277

Panigrahy, B., Aslam, M., Misra, D. S., and Bahadur, D. (2009). Polymer-mediated shape-selective synthesis of ZnO nanostructures using a single-step aqueous approach. *CrystEngComm* 11, 1920–1925. doi:10.1039/b904833m

Perdew, J. P., Burke, K., and Ernzerhof, M. (1996). Generalized gradient approximation made simple. *Phys. Rev. Lett.* 77, 3865–3868. doi:10.1103/PhysRevLett.77.3865

Pradeev raj, K., Sadaiyandi, K., Kennedy, A., Sagadevan, S., Chowdhury, Z. Z., Bin Johan, M. R., et al. (2018). Influence of Mg doping on ZnO nanoparticles for enhanced photocatalytic evaluation and antibacterial analysis. *Nanoscale Res. Lett.* 13, 229. doi:10.1186/s11671-018-2643-x

Qumar, U., Ikram, M., Imran, M., Haider, A., Ul-Hamid, A., Haider, J., et al. (2020). Synergistic effect of Bi-doped exfoliated MoS2 nanosheets on their bactericidal and dye degradation potential. *Dalt. Trans.* 49, 5362–5377. doi:10.1039/d0dt00924e

Ramola, B., and Joshi, N. C. (2019). Green synthesis, characterisations and antimicrobial activities of CaO nanoparticles. *J. Chem.* 35, 1154–1157. doi:10.13005/ojc/350333

Ramya, S., Viruthagiri, G., Gobi, R., Shanmugam, N., and Kannadasan, N. (2016). Synthesis and characterization of Ni2+ ions incorporated CuO nanoparticles and its application in antibacterial activity. *J. Mat. Sci. Mat. Electron.* 27, 2701–2711. doi:10.1007/s10854-015-4080-2

Raza, W., Haque, M. M., Muneer, M., Harada, T., and Matsumura, M. (2015). Synthesis, characterization and photocatalytic performance of visible light induced bismuth oxide nanoparticle. *J. Alloys Compd.* 648, 641–650. doi:10.1016/j.jallcom.2015.06.245

Rojas, O. J., Gómez, L. M., López, J. G., Barrera-Zapata, R., and Giraldo, S. A. (2014). Producción de biodiesel a partir de aceite de palma en un reactor de lecho fijo con metóxido de calcio como catalizador. *Ing. Y Compet.* 16, 109–118. doi:10.25100/iyc.v16i1.3717

Roy, A., Bulut, O., Some, S., Mandal, A. K., and Yilmaz, M. D. (2019). Green synthesis of silver nanoparticles: Biomolecule-nanoparticle organizations targeting antimicrobial activity. *RSC Adv.* 9, 2673–2702. doi:10.1039/c8ra08982e

Saleh, S. A., Ibrahim, A. A., and Mohamed, S. H. (2016). Structural and optical properties of nanostructured Fe-doped SnO2. *Acta Phys. Pol. A* 129, 1220–1225. doi:10.12693/APhysPolA.129.1220

Sawai, J. (2003). Quantitative evaluation of antibacterial activities of metallic oxide powders (ZnO, MgO and CaO) by conductimetric assay. *J. Microbiol. Methods.* 54, 177–182. doi:10.1016/S0167-7012(03)00037-X

Sharma, G., Prema, D., Venkataprasanna, K. S., Prakash, J., Sahabuddin, S., and Devanand Venkatasubbu, G. (2020). Photo induced antibacterial activity of CeO2/GO against wound pathogens. *Arab. J. Chem.* 13, 7680–7694. doi:10.1016/j.arabjc.2020.09.004

Singh, K. R. B., Nayak, V., Sarkar, T., and Singh, R. P. (2020). Cerium oxide nanoparticles: Properties, biosynthesis and biomedical application. *RSC Adv.* 10, 27194–27214. doi:10.1039/d0ra04736h

Singhal, G., Bhavesh, R., Kasariya, K., Sharma, A. R., and Singh, R. P. (2011). Biosynthesis of silver nanoparticles using Ocimum sanctum (Tulsi) leaf extract and screening its antimicrobial activity. *J. Nanoparticle Res.* 13, 2981–2988. doi:10.1007/s11051-010-0193-y

Sinha, S., Aman, A. K., Singh, R. K., Kr, N., and Shivani, K. (2020). Calcium oxide(CaO) nanomaterial (Kukutanda twak Bhasma) from egg shell: Green

synthesis, physical properties and antimicrobial behaviour. *Mat. Today Proc.* 43, 3414–3419. doi:10.1016/j.matpr.2020.09.072

Skrabania, K., Miasnikova, A., Bivigou-Koumba, A. M., Zehm, D., and Laschewsky, A. (2011). Examining the UV-vis absorption of RAFT chain transfer agents and their use for polymer analysis. *Polym. Chem.* 2, 2074–2083. doi:10.1039/c1py00173f

Smidstrup, S., Markussen, T., Vancraeyveld, P., Wellendorff, J., Schneider, J., Gunst, T., et al. (2020). QuantumATK: An integrated platform of electronic and atomic-scale modelling tools. *J. Phys. Condens. Matter.* 32, 015901. doi:10.1088/1361-648X/ab4007

Smirnov, I. V., Rau, J. V., Fosca, M., de Bonis, A., Latini, A., Teghil, R., et al. (2017). Structural modification of titanium surface by octacalcium phosphate via pulsed laser deposition and chemical treatment. *Bioact. Mat.* 2, 101–107. doi:10.1016/j.bioactmat.2017.03.002

Sood, S., Umar, A., Mehta, S. K., and Kansal, S. K. (2015). Highly effective Fe-doped TiO2 nanoparticles photocatalysts for visible-light driven photocatalytic degradation of toxic organic compounds. *J. Colloid Interface Sci.* 450, 213–223. doi:10.1016/j.jcis.2015.03.018

Sreekanth, T. V. M., Jung, M. J., and Eom, I. Y. (2016). Green synthesis of silver nanoparticles, decorated on graphene oxide nanosheets and their catalytic activity. *Appl. Surf. Sci.* 361, 102–106. doi:10.1016/j.apsusc.2015.11.146

Subramanian, H., Krishnan, M., and Mahalingam, A. (2022). Photocatalytic dye degradation and photoexcited anti-microbial activities of green zinc oxide nanoparticles synthesized: Via Sargassum muticum extracts. *RSC Adv.* 12, 985–997. doi:10.1039/d1ra08196a

Tahir, N., Zahid, M., Bhatti, I. A., and Jamil, Y. (2022). Fabrication of visible light active Mn-doped Bi2WO6-GO/MoS2 heterostructure for enhanced photocatalytic degradation of methylene blue. *Environ. Sci. Pollut. Res.* 29, 6552–6567. doi:10.1007/s11356-021-16094-5

Tangboriboon, N., Kunanuruksapong, R., Sirivat, A., Kunanuruksapong, R., and Sirivat, A. (2012). Preparation and properties of calcium oxide from eggshells via calcination. *Mat. Sci. Pol.* 30, 313–322. doi:10.2478/s13536-012-0055-7

van Setten, M. J., Giantomassi, M., Bousquet, E., Verstraete, M. J., Hamann, D. R., Gonze, X., et al. (2018). The PSEUDODOJO: Training and grading a 85 element optimized norm-conserving pseudopotential table. *Comput. Phys. Commun.* 226, 39–54. doi:10.1016/j.cpc.2018.01.012

Vanthana Sree, G., Nagaraaj, P., Kalanidhi, K., Aswathy, C. A., and Rajasekaran, P. (2020). Calcium oxide a sustainable photocatalyst derived from eggshell for efficient photo-degradation of organic pollutants. *J. Clean. Prod.* 270, 122294. doi:10.1016/j.jclepro.2020.122294

Walter, M. G., Warren, E. L., McKone, J. R., Boettcher, S. W., Mi, Q., Santori, E. A., et al. (2010). Solar water splitting cells. *Chem. Rev.* 110, 6446–6473. doi:10.1021/cr1002326

Wang, L., Hu, C., and Shao, L. (2017). The antimicrobial activity of nanoparticles: Present situation and prospects for the future. *Int. J. Nanomedicine.* 12, 1227–1249. doi:10.2147/IJN.S121956

Yang, C. C., Chien, W. C., Chen, P. W., and Wu, C. Y. (2009). Synthesis and characterization of nano-sized calcium zincate powder and its application to Ni-Zn batteries. *J. Appl. Electrochem.* 39, 39–44. doi:10.1007/s10800-008-9637-9

Zaaba, N. I., Foo, K. L., Hashim, U., Tan, S. J., Liu, W. W., and Voon, C. H. (2017). "Synthesis of graphene oxide using modified hummers method: Solvent influence," in *Procedia Eng., No longer published by* (Elsevier), 469–477. doi:10.1016/j.proeng.2017.04.118

Zhu, J., Zheng, W., He, B., Zhang, J., and Anpo, M. (2004). Characterization of Fe-TiO2 photocatalysts synthesized by hydrothermal method and their photocatalytic reactivity for photodegradation of XRG dye diluted in water. *J. Mol. Catal. A Chem.* 216, 35–43. doi:10.1016/j.molcata.2004.01.008